Development & Experimental Assessment of a Live-load Moment Continuity

Final Report
June 2025

Principal Investigator: William G Davids, PhD, PE

Bodwell University Distinguished Professor & Chair
of Civil and Environmental Engineering
University of Maine

Authors: William G. Davids[1] and Marlon Marin-Quintero[2]

[1]Department of Civil and Environmental Engineering, University of Maine, 5711 Boardman Hall, Orono, Maine, USA, 04469-5711
[2]Advanced Structures and Composites Center, University of Maine, 35 Flagstaff Road, Orono, Maine, USA, 04469-5793

Sponsored By

TIDC
Transportation Infrastructure Durability Center
AT THE UNIVERSITY OF MAINE

A report from
The University of Maine
Advanced Structures & Composites Center
35 Flagstaff Road
Orono, ME, 04469
Phone: 207-581-2123
composites.umaine.edu/

About the Transportation Infrastructure Durability Center

The Transportation Infrastructure Durability Center (TIDC) is the 2018 US DOT Region 1 (New England) University Transportation Center (UTC) located at the University of Maine Advanced Structures and Composites Center. TIDC's research focuses on efforts to improve the durability and extend the life of transportation infrastructure in New England and beyond through an integrated collaboration of universities, state DOTs, and industry. The TIDC is comprised of six New England universities, the University of Maine (lead), the University of Connecticut, the University of Massachusetts Lowell, the University of Rhode Island, the University of Vermont, and Western New England University.

U.S. Department of Transportation (US DOT) Disclaimer

Acknowledgements

Funding for this research is provided by the Transportation Infrastructure Durability Center at the University of Maine under grant 69A3551847101 from the U.S. Department of Transportation's University Transportation Centers Program. [Include any acknowledgements for other contributors (i.e. your university or contributing DOTs/industry partners) here.]

Contents

List of Figures

List of Tables

List of Key Terms

FRP composite bridge girder; continuous bridge girder; shear friction; experimental testing; FRP compression buckling

Abstract

During 2021-2024, four vehicular bridges have been constructed using hybrid, fiber-reinforced polymer (FRP) composite tub (CT) girders in the United States. However, these bridges are single-span, simply supported structures, and wider application of the CT girder will require adapting it to continuous, multi-span configurations to increase design efficiency, reduce live load deflections, and improve serviceability. Indeed, two multi-span, continuous CT girder bridges are currently under construction, but their success hinges on the development of a live load continuity joint to carry negative moments at interior piers and integral abutments. While live load continuity joints are routinely used and well-understood for precast concrete girder bridge construction, their implementation in CT girder bridges is not straightforward due to the requirement that FRP bottom flange compressive stresses be transferred between discontinuous girder ends. This study directly addresses this challenge through the development of a novel CT girder live-load continuity joint that relies on a short length of concrete infill within adjacent discontinuous girders. The concrete is mechanically bonded to the purposely deformed girder interior via shear-friction, while the girder serves as concrete formwork, easing construction. A rational design methodology is presented to determine the necessary length of concrete infill given a required moment capacity and girder cross-section while also accounting for flange compressive buckling. A heavily instrumented, large-scale prototype is tested to failure to assess joint performance, and measured strains are compared with calculated values. The efficiency gains made possible by the live load continuity joint are then assessed via a realistic design scenario. The joint exhibited 11.4% more moment capacity than predicted based on the expected failure stress at the FRP-concrete shear-friction interface. The design example showed that live load continuity results in a significant reduction in girder depth and the amount of carbon fiber needed in the girder compression flange.

Chapter 1: Introduction and Background

1.1 Project Motivation

Fiber-reinforced polymer (FRP) materials can be attractive for bridge construction due to their inherent corrosion resistance and light weight. Internal FRP concrete reinforcement has seen significant research and development (Benmokrane et al. 2006; Bakis et al. 2002; Kassem et al. 2011; Bentz et al. 2010), and its application is covered in several design codes (AASHTO 2012; AASHTO 2018; ACI 2015; ACI 2017). Structural FRP members have also been used in the construction of pedestrian bridges (Skinner 2009; Li et al. 2014, Sá et al. 2017; Bai and Keller 2008; Mendes et al. 2011), and in the United States their design is governed by the AASHTO *Guide Specifications for the Design of FRP Pedestrian Bridges* (AASHTO 2008). While a number of earlier studies have examined the potential use of FRP girders in vehicular bridges (Burgueño 1999; Karbhari et al. 2000; Honickman and Fam 2009; Fam and Honickman 2010), they have seen little in-service use as the main superstructure members in vehicular bridges, and their design is not governed by existing codes. To-date, one FRP girder bridge has been constructed in Spain (Gutierrez et al. 2008; Mieres et al. 2007) and one in Poland (Siwowski et al. 2017; Siwowski and Rajchel 2019). In the United States, four FRP composite tub (CT) girder bridges have been built since 2021 (Pinkham et al. 2024; Davids et al. 2022a), indicating growing acceptance of this technology. For reference, Figure 1 shows an image of an in-service CT girder bridge and elements of a typical CT girder cross-section composed of foam-core webs with +/-45 degree E-glass face sheets, shear connectors between the concrete deck and girder, and a largely unidirectional carbon fiber bottom flange.

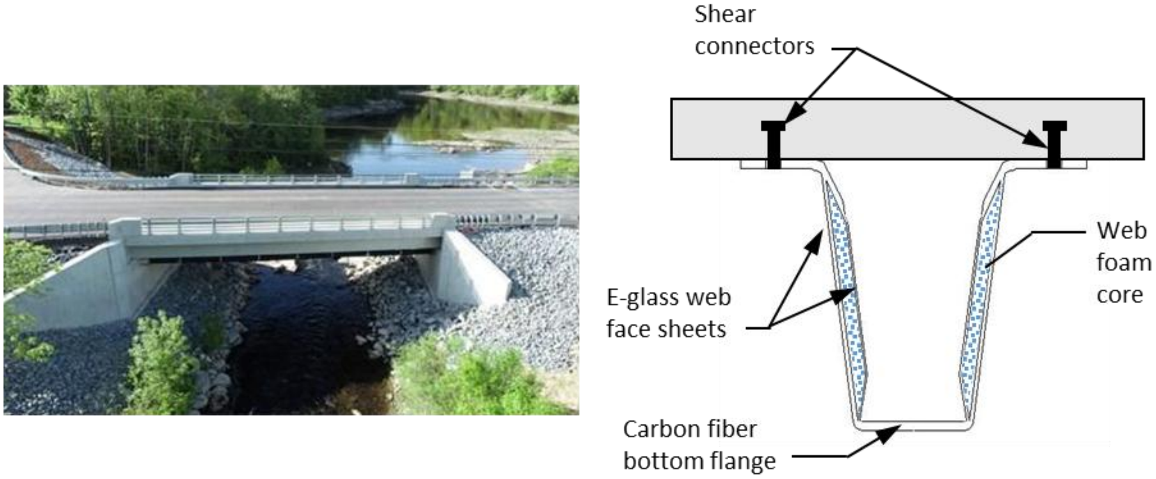

a) Hampden, Maine CT girder bridge

b) Elements of a CT girder cross-section

Figure 1: In-Service CT girder bridge and typical CT girder cross-section

While critical aspects of CT girder response – including girder flexural strength and fatigue resistance (Davids et al. 2022a; Davids et al. 2024), girder-deck shear connector behavior (Davids et al. 2022b), web shear strength and buckling (Schanck et al. 2023) and live load moment and shear distribution (Pinkham et al. 2024; Pinkham et al. 2025) – have been examined, all four bridges built to-date in the United States are simple span structures. However, two adjacent multi-span CT girder bridges are presently under construction as part of a single project in Old Town, Maine over the Stillwater River. The first bridge is a 46 m long, two-span structure and the second is a 90 m long, three-span bridge. These bridges will carry two lanes of traffic and approximately 16,000 vehicles per day, and incorporate fully integral abutments with reinforced concrete-filled FRP pipe pile-supported intermediate piers. Successful use of CT girders in these structures requires that they be installed as simple spans prior to the deck pour, with live load moment continuity joints constructed at the intermediate piers and integral abutments. The live load continuity joints will reduce deflections by increasing flexural stiffness while lowering maintenance costs by eliminating deck joints at the piers and abutments.

Live load continuity joints are routinely used in precast concrete girders, with early examples including Tennessee's Big Sandy River Bridges built in the 1960s, which have exhibited excellent performance (Freyermuth 1969). Continuity joints must have sufficient flexural capacity to carry moments due to both live load and superimposed dead loads. While the design of live load continuity joints for multi-span precast concrete girder construction has been widely researched (Miller et al. 2004; Okeil and Alaywan 2011; Saadeghvaziri et al. 2004; Oesterle et al. 1989), is well understood, and is explicitly addressed by the AASHTO LRFD *Bridge Design Specifications* (2024), no FRP girder highway bridge constructed thus far has incorporated a continuity joint to the best of the authors' knowledge. Unlike a precast concrete girder, where negative moment flexural compressive stresses can be easily carried by cast-in-place concrete, an

FRP CT girder subjected to negative moment will experience large compressive stresses in the mostly unidirectional carbon fiber bottom flange that must be transferred across the joint. While the bottom flange of the CT girder can be sized to carry this compressive stress, directly connecting the bottom flanges of girders pairs terminating at an intermediate pier poses a significant design challenge that is not covered by current specifications and codes. Similarly, ensuring a reliable moment connection between an integral abutment and FRP CT girder requires the transfer of moment from the FRP section to a reinforced concrete section. However, if such a splice is successfully developed, it will offer a pathway to more efficient and durable multi-span CT girder bridges.

1.2 Research, Objectives, and Tasks

The research presented here directly addresses this challenge through the rational development and large-scale experimental assessment of a novel live load continuity joint. At interior piers, the joint relies on concrete infill over a short region of the span that is mechanically bonded to the inside of the FRP section using a frictional shear connection similar to that currently used to fasten the concrete deck to the girders (see Davids et al. 2022b for details of the girder-deck connection). The same live load splice at the interior piers can also be applied at integral abutments. In this study, the splice concept and design method are first developed, and a large-scale joint specimen is sized for a typical 30.48 m long, two-span CT girder bridge made continuous for live load. To assess joint performance, the specimen is subsequently fabricated, subjected to service level fatigue loading, and loaded to failure. The potential FRP material savings and enhanced serviceability resulting from the live load continuity joint are then explored using a realistic design scenario to illustrate the practical benefits of the connection.

1.3 Report Overview

This report is organized into four sections including this introductory section and eight subsequent sections describing the background, testing details, and major conclusions drawn in this work. These are:

- Section 2: Continuity Joint Configuration and Design Methodology
- Section 3: Details of Specimen Design and Construction
- Section 4: Specimen Test Protocols and Instrumentation
- Section 5: Experimental Results
- Section 6: Comparison between Predicted and Measured Response
- Section 7: Practical Impact of Live Load Continuity
- Section 8: Summary and Conclusions
- Section 9: Acknowledgements

Chapter 2: Continuity Joint Configuration and Design Methodology

The proposed continuity joint is shown schematically in Figure 2. It relies on concrete infill within the girder section for a length L_s that is cast with the deck concrete and confined with an internal, non-structural bulkhead. Since the open girder section acts as a concrete form and typical CT girder construction requires a full-width diaphragm at supports, additional field-installed formwork is minimal, making it simple to fabricate. Beyond the end of the splice at the bulkhead, the girder, deck and deck reinforcing carry the full moment and shear within the span.

However, at the pier centerline, abutting girders are discontinuous, and moment due to superimposed live and dead load is carried by a reinforced concrete section that results in the usual stress resultants C_c from concrete in compression and T provided by additional deck reinforcement in tension (see Figure 2). The key to success of the splice is the transfer of bending compression stress in the girder bottom flange, which is largest at the bulkhead, to the concrete infill. This is accomplished through interface shear stresses f_v between the interior of the girder and the concrete infill (see Figure 2) that are developed via shear friction.

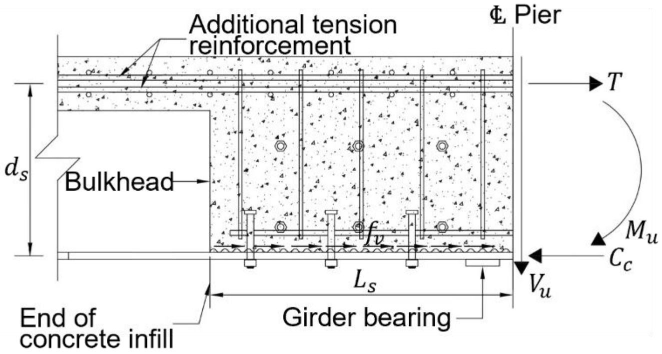

Figure 2: Continuity joint elevation and definitions

As illustrated in Figure 3, CT girders rely on 6.4 mm amplitude sinusoidal ridges infused to the top flanges and stainless steel or galvanized fasteners embedded in the deck to ensure composite action between the deck and girder through mechanical interlock. Prior compression-shear experiments have shown that an average interface shear stress at failure of $f_v = 4.12$ MPa can be reliably achieved using typical bridge deck concrete mixes and 25.4 mm diameter A325 or stainless steel studs spaced at 305 mm on center on a 152 mm wide by 559 mm long flange plates (Davids et al. 2022b). A recent full-scale strength test of a CT girder subjected to four-point bending with A325 shear studs spaced at 305 mm on center verified a similar level of shear stress transfer from the deck to the FRP girder flange prior to CT girder flexural failure (Davids et al. 2024). This implies that if the same ridges can be infused on the inside of the girder over the length L_s with shear studs passing through the shear plane with a similar interface tributary area to that used in prior testing, a value of $f_v = 4.12$ MPa can be achieved within the continuity joint.

Figure 3: CT girder top flange ridges and stainless-steel shear studs

Given f_v, the one unknown parameter to be determined for the splice design is the length of the concrete infill L_s. To accomplish this, the full concrete compressive resultant $C_c = {}^{M_u}/_{d_s}$ is assumed to be transferred to the bottom flange through f_v, where M_u is the factored negative moment at the pier centerline and d_s is the internal lever arm from the deck tension steel to the middle of the bottom flange (see Figure 2). Denoting the width of bottom flange over which the shear transfer takes place by b_s and using a strength reduction factor $\phi = 0.9$ (a typical value for shear-friction transfer in reinforced concrete), the length of splice can be computed using Equation 1. It must be noted that the design process is iterative, since the concrete infill increases the flexural rigidity of the section, and increasing L_s thus increases M_u in an indeterminate girder with two or more spans.

$$L_s = \frac{M_u}{0.9 f_v b_s d_s} \qquad \text{Eq. 1}$$

In simple span applications, the CT girder bottom flange, which is laminated from unidirectional carbon fiber and +/- 45 degree E-glass web face sheets that are anchored in flange, is optimized for tensile strength and stiffness. However, at L_s from the pier centerline, the bottom flange will experience large compressive stresses due to negative moment. This implies that buckling of the CT girder compression flange must be checked as part of the splice design. To assess this, the critical compressive buckling load resultant of the compression flange N_{cr}, which must be divided by the flange thickness to give the buckling stress, was calculated according to the analytical model of Qiao & Zou (2002) given in Equations 2-6. These equations were developed specifically to predict compressive buckling of compression flanges in FRP box beams, and are therefore directly applicable to the CT girder adjacent to the splice. In Equations 2-6, D is the bending stiffness matrix of the laminate determined with classical lamination theory, and b is the width of the plate. The superscripts f and w refer to the properties of the compression flange and webs, respectively.

$$N_{cr} = \frac{24}{b^2}\left[1.871\sqrt{\frac{\tau_2}{\tau_1}}\sqrt{D_{11}D_{22}} + \frac{\tau_3}{\tau_1}(D_{12} + 2D_{66})\right] \qquad \text{Eq. 2}$$

$$\tau_1 = 124 + 22\chi + \chi^2, \quad \tau_2 = 24 + 14\chi + \chi^2, \quad \tau_3 = 102 + 18\chi + \chi^2 \qquad \text{Eq. 3}$$

$$\chi = \frac{D_{22}^w}{D_{22}^f}\frac{r}{\rho\left({}^{b^w}/_{b^f}\right)} \qquad \text{Eq. 4}$$

$$r = 1 - \frac{(b^w)^2}{(b^f)^2}\frac{\left[\sqrt{D_{11}^f D_{22}^f} + D_{12}^f + 2D_{66}^f\right]}{\left[\sqrt{D_{11}^w D_{22}^w} + D_{12}^w + 2D_{66}^w\right]} \qquad \text{Eq. 5}$$

$$\rho\left({}^{b^w}/_{b^f}\right) = \frac{1}{\pi}tanh\left(\frac{\pi b^w}{2b^f}\right)\left[1 + \frac{2b^w/_{b^f}}{sinh\left(\pi b^w/_{b^f}\right)}\right] \qquad \text{Eq. 6}$$

Equations 2-6 account for partial rotational restraint provided to the compression flanges by the webs, which is quantified by the elastic restraint coefficient χ. A simple, conservative approach is to set $\chi = 0$, which corresponds to the compression flange having simply supported edges. For this case N_{cr} is given by Eq. 7 (Qiao and Zou 2002).

$$N_{cr} = \frac{19.742}{b^2}\left[\sqrt{D_{11}D_{22}} + D_{12} + 2D_{66}\right] \qquad \text{Eq. 7}$$

Chapter 3: Details of Specimen Design and Construction

3.1 Model Structure and Girder Section

The cross-section of the model structure used for the continuity joint specimen design is illustrated in Figure 4a and details of an individual girder cross-section are shown in Figure 4b. The model structure deck width and girder spacing are identical to those of an 11.58 m simple span CT girder bridge constructed in Westerly, Rhode Island in 2022, and the Westerly live load moment and shear distribution factors of 0.69 lanes of live load per girder were used to size a typical interior girder. However, the model structure is a continuous bridge with two, 15.24 m spans, and the girder has a wider bottom flange to provide a larger width b_s over which shear transfer occurs. Roller supports are assumed at each abutment, which will maximize negative moment at the interior pier live load continuity joint. These dimensions correspond to an overall span-to-depth ratio of 20.3, which is 22.4% greater than that of the simple span Westerly, RI structure. The girder dimensions also correspond to an approximately 2/3 scale version of the girders in the two-span bridge currently under construction in Old Town, Maine, which will be deeper but have the same bottom flange width. The maximum Strength I interior girder negative moment and shear at the pier centerline were calculated using the provisions of AASHTO (2024) and the MaineDOT (2018) to be $M_u = 1447$ kN-m and $V_u = 447$ kN, respectively. We note here that the MaineDOT requires bridges to be designed for Strength I assuming a truck that is 25% greater than the AASHTO-specified HL-93 vehicle.

The CT girder section shown in Figure 4b features foam-core webs with +/-45 degree E-glass web face sheets for shear strength that are integrated into the top and bottom flange layup and unidirectional carbon fiber in the bottom flange for bending strength and stiffness. The bottom flange thickness and number of bottom flange carbon plies were constant along the span. The girder was fabricated using vinyl-ester resin and vacuum-infusion. The concrete deck had a nominal compressive strength of 28 MPa and conformed with a typical MaineDOT Class I mix used for bridge deck construction. The 28-day compressive strength was 43 MPa based on three cylinder tests, and the compressive strength was 51 MPa based on three cylinder tests at the time the specimen was loaded to failure (103 days after casting). The webs were designed for both shear strength and shear buckling based on the procedure described by Schanck et al. (2023).

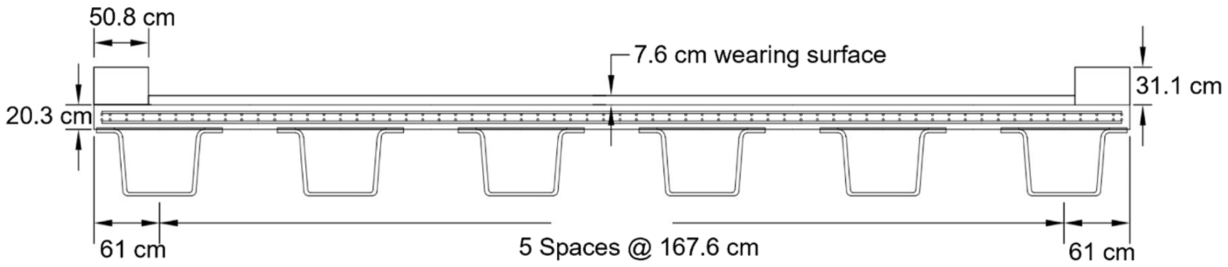

(a) Model structure cross section

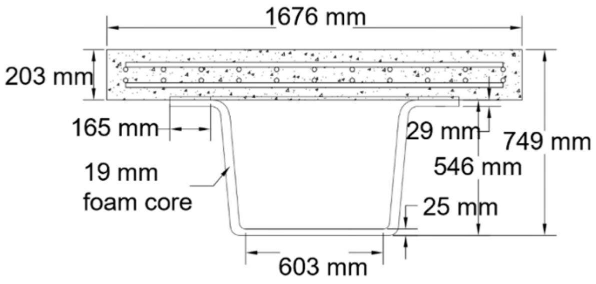

(b) Specimen cross section

Figure 4: Details of model structure and CT girder cross-section

Linearly elastic behavior was assumed for all FRP sections in the girder. Classical lamination theory was used to determine the critical material properties including the longitudinal modulus (E_1), transverse modulus (E_2), Poisson's ratio (υ_{12}) and shear modulus (G_{12}) for each portion of the CT girder section as given in Table 1. Zones 1-3 correspond to regions of the girder with different web layups that were necessary to support concentrated forces, and their locations are given later. Details of the design methodology for this section can be found in Davids et al. (2024), and a recent test of a similar section for positive bending strength when used for an 11.58 m simple span showed it had a capacity of approximately twice the factored AASHTO Strength I moment. This large apparent over-strength is due to the use of significant capacity reduction factors to account for statistical reliability and environmental degradation of the FRP as well as the usual strength reduction factor.

Table 1: Test Specimen Properties

	Zone 1				
	E_1 (GPa)	E_2 (GPa)	ν_{12}	G_{12} (GPa)	t (mm)
Compression Flange	74.32	9.83	0.24	8.35	25
Web Face Sheets	17.28	17.21	0.28	8.07	26
Bottom Flange	30.58	12.00	0.24	6.10	29
	Zone 2				
	E_1 (GPa)	E_2 (GPa)	ν_{12}	G_{12} (GPa)	t (mm)
Compression Flange	74.32	9.83	0.24	8.35	25
Web Face Sheets	14.57	14.57	0.28	10.11	18
Bottom Flange	30.58	12.00	0.24	6.10	29
	Zone 3				
	E_1 (GPa)	E_2 (GPa)	ν_{12}	G_{12} (GPa)	t (mm)
Compression Flange	74.32	9.83	0.24	8.35	25
Web Face Sheets	17.28	17.21	0.28	8.07	26
Bottom Flange	30.58	12.00	0.24	6.10	29

3.2 Continuity Joint Test Specimen Details

For the design of the test specimen, 532 mm wide sinusoidal ridges were assumed over the interior surface of the compression flange with $d_s = 630$ mm. Using these dimensions and a typical value of $f_v = 4.12$ MPa, the required splice length L_s was computed iteratively using Equation 1 to be 1.14 m, or 7.5% of the span length. The specimen was ultimately fabricated with L_s = 1.14 m to carry the corresponding Strength I factored moment M_u of 1447 kN-m. **Error! Reference source not found.**5 shows a photo of the ends of the two, 3.35 m long girder sections used to make the jointed specimen with ridges infused on the interior and top flanges. During specimen fabrication, a 75 mm wide center section of the interior of the bottom flange was created without ridges to promote infusion. This reduced b_s from the assumed value of 532 mm to 457 mm, which is accounted for in subsequent analyses of the test results. Further, to promote continuity between the full depth of the FRP section and concrete infill, vertical ridges were also infused on the interior surface of the webs over a height of 457 mm as shown in Figure 5. The girder was fabricated as a single member and then cut in half to make it discontinuous prior to casting the deck, continuity joint, and diaphragms with a single pour. As shown in Figures 5 and 6, the bottom flange had 12, 25 mm diameter A325 bolts anchoring the concrete to the bottom flange, which corresponds to a bottom flange ridge area tributary to each fastener of 435 cm^2. This is 2.3% more than the 425 cm^2 tributary to each fastener in the compression-shear tests of Davids et al. (2022b). Each section of the specimen was originally drilled to accommodate 16 bolts through the bottom flange as shown below, but external nuts were not installed on the row of four fasteners closest to each end of each section to better replicate a field scenario where each girder end rests on an individual bearing. Six fasteners were used to anchor each web over half the splice length.

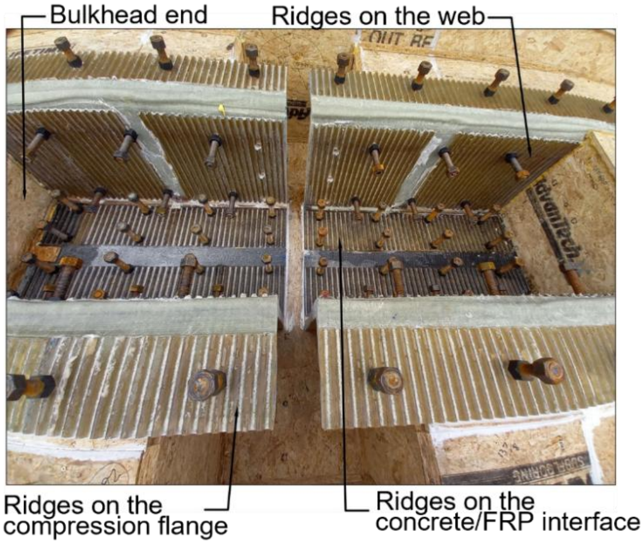

Figure 5: Girder interior photo

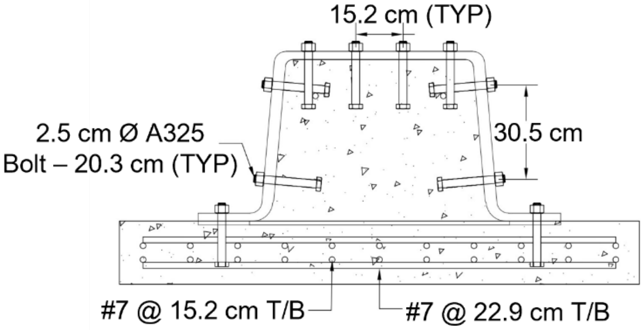

Figure 6: Test girder cross-section

As shown in Figure 6, the test configuration oriented the specimen with the deck on the bottom, which allowed the application of a negative moment in the actual girder orientation using a compressive load from a hydraulic actuator (more details of load application are provided in the next section). Each one of the two CT girder sections terminated at approximately 38 mm from the specimen mid-span to mimic a normal construction detail and ensure there was no direct bearing between the two girder bottom flanges (refer to Figure 5). A full-width, 45.7 cm thick diaphragm was cast at mid-span and 61 cm diaphragms cast at the girder ends over the full depth of the specimen, which is typical for CT girder bridge construction. The longitudinal deck reinforcing consisted of 22-#7 bars with a specified yield strength of 414 MPa, which provided a moment capacity $\emptyset M_n$ at pier centerline of 1641 kN-m, 13.4% greater than the Strength I moment of 1447 kN-m. While slightly less tensile reinforcing could have been used, the excess flexural capacity was purposeful to allow larger stresses f_v to be applied to the girder-concrete interface prior to failure. Two #6 bars were included in the infill region near the carbon fiber compression flange to promote handling of the girder, as all concrete was cast with the deck on top before the specimen was flipped for testing as oriented in Figures 6 and 7. Code-minimum stirrups were also included within the splice, and according to AASHTO (2024) the reinforced concrete section had sufficient shear strength to carry the full Strength I factored shear force $V_u = 447$ kN.

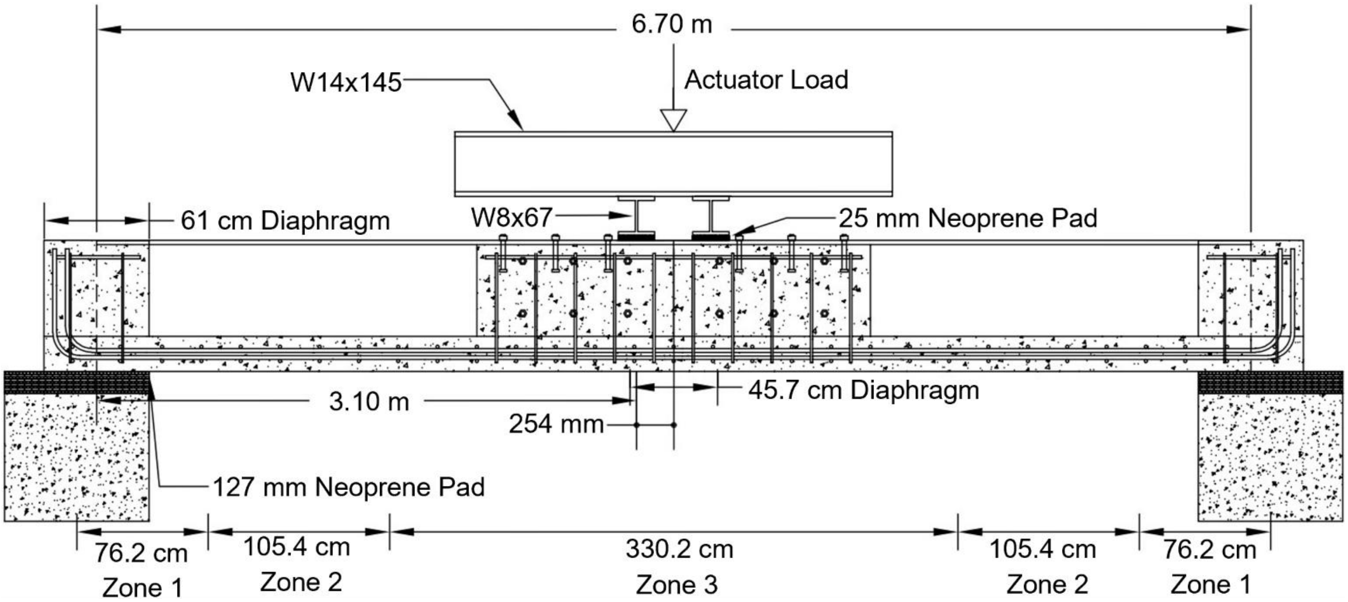

Figure 7: Four Point Bending Test Configuration

Material properties for the three girder zones denoted in Figure 7 are given in Table 1. Zone 2 was a typical CT girder section with the 19 mm thick foam-core web shown Figure 4b, whereas Zone 3 had a solid web where the foam core was replaced with six extra fiberglass plies. The solid web of Zone 3 was purposely extended approximately one girder depth beyond the end of the concrete infill region to promote good stress transfer over the full continuity joint length and avoid an abrupt transition of the FRP girder section at the start of the concrete infill. Zone 1 included both the foam-core and the six extra glass plies, which is typical at CT girder simple supports to ensure that the web can carry concentrated reactions without crippling or excessive local deformation.

Buckling of the compression flange was checked using Equation 2 (partially restrained edges) and Equation 7. Compression flange stresses were computed using a simple transformed section analysis and the elastic moduli of the flanges and webs given in Table 1 for Zone 3, which is adjacent to the bulkhead. The concrete deck was assumed to be fully cracked, and the deck reinforcement was included when computing the location of the section neutral axis and transformed moment of inertia. The peak Strength I moment at the splice bulkhead in the two-span model bridge of 1117 kN-m was used to compute the factored compression flange stress of 108 MPa. The most conservative buckling resultant $N_{cr} = 3.37$ kN/mm given by Equation 7 corresponds to a compression flange stress of 134.8 MPa when divided by its thickness of 25 mm. This implies that the compression flange had at least a 24.8% reserve buckling capacity relative to the Strength I stress. Equation 2 predicts a buckling stress of 157.3 MPa, which is 45.6% greater than the Strength I stress.

One final design-related detail is the specimen span length of 6.7 m, which was chosen to ensure that the ratio of moment to shear in the specimen reflected that experienced by the two-span model bridge. The 6.7 m span length and load configuration in Figure 7 require an actuator load of 934 kN to produce the peak Strength I M_u of 1447 kN-m. This corresponds to a specimen shear of 467 kN, which is 4.5% more than the Strength I V_u of 447 kN that will occur in the two-span model bridge under the loading producing $M_u = 1447$ kN-m.

Chapter 4: Specimen Test Protocols and Instrumentation

As shown in Figure 7 the test specimen was subjected to four-point bending with closely spaced load heads using a 2000 kN hydraulic actuator. The actuator applied the load to a W13x145 spreader beam, which transferred it to two transverse W8x67 load beams. Each W8x67 load beam spanned the width of the diaphragm and was continuously supported by a 25 mm thick neoprene bearing pad. The load beams were spaced at 508 mm to mimic locations of individual bearings on which each girder would rest in an actual bridge. The end diaphragms were supported on 127 mm thick neoprene bearing pads to allow free rotation.

During testing, longitudinal strain gauges and string potentiometers were used to monitor the specimen's behavior as shown in Figures 8 and 9. A pair of string potentiometers were located at mid-span and near each support of the specimen. The total applied load was recorded through the actuator's internal load cell. The mid-span string potentiometers recorded mid-span deflections and the ones near each end were intended to capture neoprene bearing pad compression.

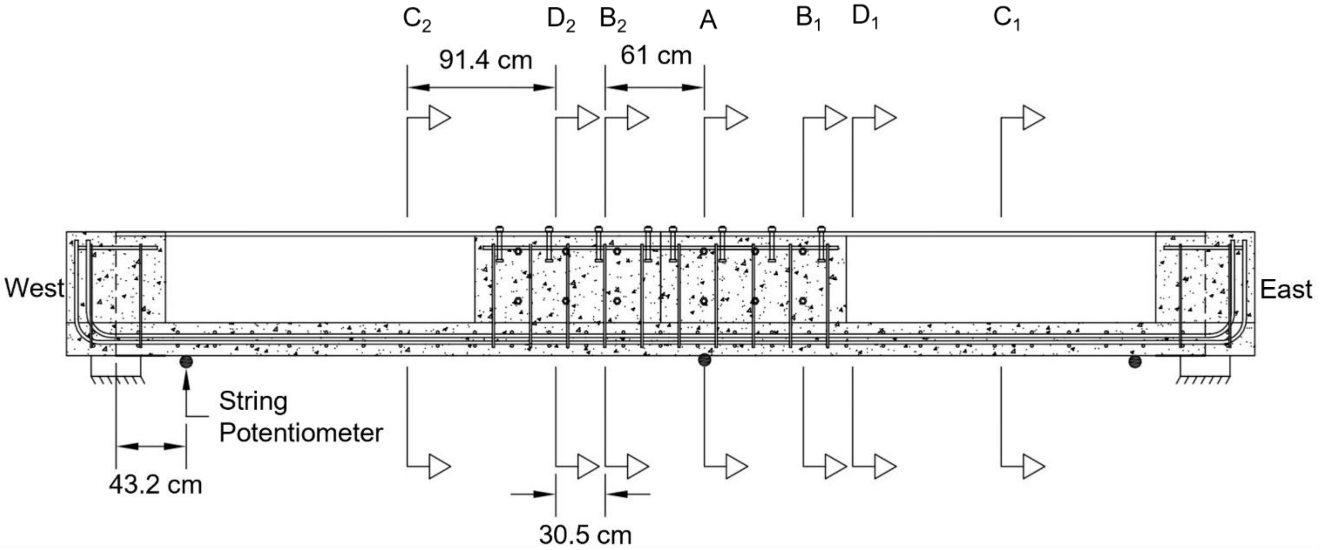

Figure 8: Layout of instrumented sections

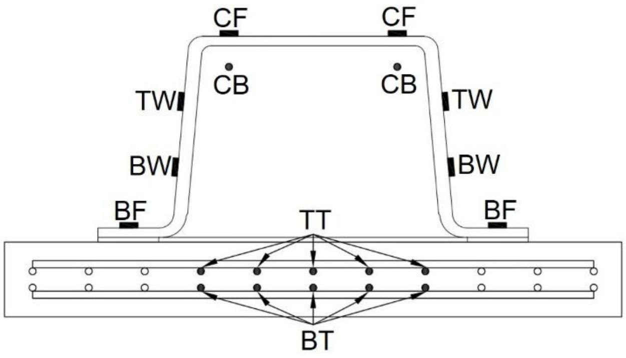

Figure 9: Reference section and gauge locations

As shown in Figures 8 and 9, multiple uniaxial strain gauges were installed at seven different cross-sections to track longitudinal flexural strains along the length and over the depth of the specimen. Section C allowed the assessment of strains over the depth of the FRP section outside the splice region. Sections B and D were instrumented to assess the transfer of stress from the FRP section to the reinforced concrete infill at different locations along the splice. Finally, section A was instrumented to explore the behavior of the midspan reinforced concrete section where no FRP is present. As shown in Figure 9, strain gauge instrumentation at sections B and D included 10 gauges on the deck longitudinal rebar, gauges on each compression rebar, and eight gauges on the FRP section. Sections C that were outside the continuity joint region did not include the gauges in the compression bars, and section A of course could not include the FRP girder gauges. The acronyms used for the gauges are BT for bottom deck tension bars, TT for deck top tension bars, BF for girder bottom flange, BW for girder bottom web gauges, TW for girder top web, CB for compression reinforcing bars, and CF for the compression flange (Figure 8). When reporting strain results in section 5, the notation employed for the gauges at each cross-section is defined as follows. The two letters indicate the gauge location within the cross-section (refer to Figure 9), while the number at the end corresponds to the longitudinal location, where section labels ending in “1” are located in the east part of the specimen and section labels ending in “2” are located in the west part of the specimen (refer to Figure 8).

Prior to testing the specimen to failure, it was subjected to slightly more than 500,000 cycles of an AASHTO Fatigue II loading. This loading was not intended to assess fatigue capacity, but only to shake down the specimen. Prior compression-shear tests of the ridged shear-friction girder-deck connection (Davids et al 2022b) have demonstrated excellent fatigue behavior and post-fatigue strength, and therefore fatigue is not a design concern for this aspect of the joint detail. Per AASHTO requirements, the fatigue load range was determined for the two-span continuous model structure using a single HL-93 truck and 0.5 lanes of fatigue live load, which resulted in a 223 kN-m fatigue moment for the specimen. To account for additional dead load from a 76 mm asphalt layer and self-weight, additional moments equal to 93.7 kN-m and 93.1 kN-m, respectively, were used to calculate the fatigue load range. Taking into account the four-point bend configuration (Figure 7) and the specimen self-weight, mimicking this required an applied load range of 0.4 kN to 205 kN. However, due to the need to have a larger lower limit load applied by the actuator to ensure target load levels were met, the load limits were set to 13.3 kN and 218 kN. The fatigue cycles were applied using a sinusoidal ramp at a rate of 1 Hz, requiring approximately 6 days to complete. Strain readings were not taken during the fatigue loading.

Following fatigue testing, the specimen was subjected to several cycles of increasing service load before being driven to failure. First, three initial load cycles of 236 kN were applied to generate a moment equivalent to half of an AASHTO Service I limit state to settle the specimen. Then, three cycles of a 472 kN actuator load were applied that generated a midspan moment equivalent to that caused by an AASHTO Service I loading on the model two-span continuous bridge. Following this, the specimen was loaded monotonically until failure.

Chapter 5: Experimental Results

5.1 Response to Fatigue Loading

Figure 10 presents the mid-span girder displacement recorded by string potentiometers over the 514,863 fatigue cycles applied to the specimen. In addition to displacements due to minimum and maximum load limits, displacement caused by the fatigue load range is given to provide insight into how the girder accumulates permanent deflection. Over the first 200,000 cycles, the overall displacement increases by about 0.5 mm. However, this could be due to accumulating permanent compression of the neoprene pads at the supports, and early deformations such as this are typical as a specimen and its supports settle during cyclic loading. After around 200,000 cycles, there were very small fluctuations in mid-span displacements, with deflections due to the fatigue range consistently oscillating between 0.63 mm and 0.70 mm.

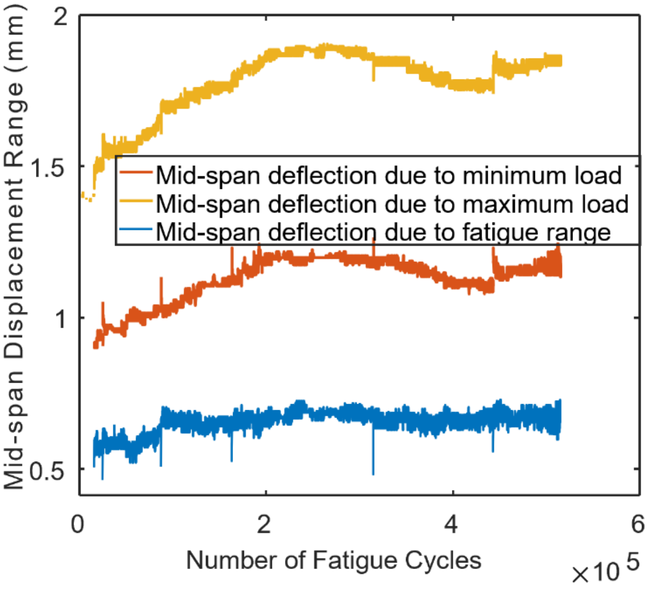

Figure 10: Mid-span displacement due to Fatigue range load

5.2 Load-Displacement Response and Observed Failure

Figure 11 shows the load-displacement response of the specimen for all cycles of post-fatigue loading. One cycle to 311 kN was inadvertently applied due to an operator error prior to loading the specimen to the full Service I load. It took approximately 30 seconds for each 50% Service I cycle, and 1 minute for each Service I cycle to be completed. After the last application of Service I load, the loading regime was switched from load to displacement control, but due to a second operator error the specimen was inadvertently loaded to failure at a rate of approximately 270 mm/minute. While this load rate is faster than desired, a subsequent review of the strain information in both the FRP and concrete indicated strain rates that were quasi-static for reinforced concrete (Zhang and Abedini 2023). Other research indicates that strain rates produced in the FRP were either at or only slightly above the limit of quasi-static (Ma et al. 2021; Cao et al. 2020; Jendli 2009) or below the quasi-static limit (Nejad et al. 2021). Further, the overall specimen stiffness (slope of the load-deflection curve in Figure 11) is essentially identical during both loading to Service I and while loading to failure. Based on this, dynamic and viscoelastic effects were insignificant despite the rapid rate of loading.

At the beginning of each cycle, and after reaching each peak of the cycle and beginning unloading, the string potentiometers did not record correctly, essentially giving a constant reading despite the initial change in load. Because of this, it was not possible to determine a true mid-span displacement by subtracting the average support displacement from the measured mid-span string pot reading, and Figure 11 therefore only reports the uncorrected mid-span string pot reading. The apparent permanent deflection occurring after the first cycle of each load level is attributed to compression of the neoprene layer at the supports.

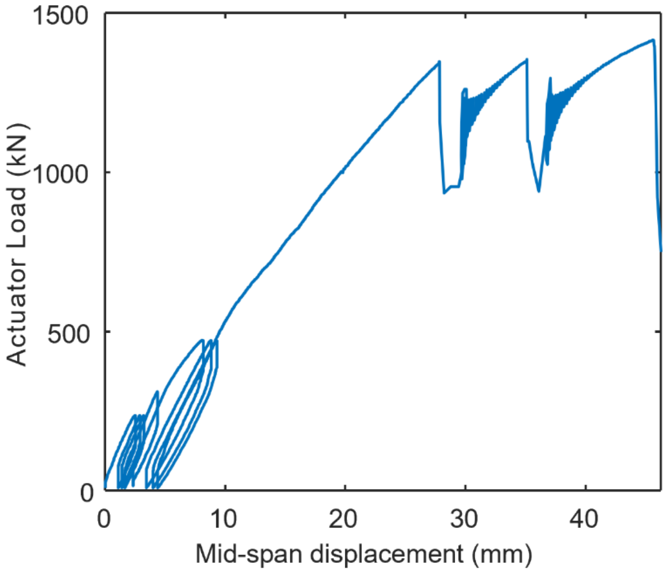

Figure 11: Load-Displacement Response of Specimen

The first failure occurred due to buckling of the compression flange near the west end of the splice at a load of 1348 kN as indicated by the first peak in Figure 11. The load of 1348 kN, when combined with the specimen self-weight, produced a mid-span moment of 2181 kN-m, which is 50.7% greater than the 1447 kN-m AASHTO Strength I moment and 19.6% greater than the 1824 kN-m nominal moment capacity M_n of the midspan reinforced concrete section. This was followed by a similar buckling failure in the compression flange near the east end of the splice that was smaller but visible over the compression flange width at the second peak load of 1355 kN. Ultimately, at 1416 kN the original buckling failure in the west section of the specimen progressed to a complete fracture of the compression flange and webs (refer to Figures 12 and 13). A video of the specimen taken during testing confirmed this failure sequence.

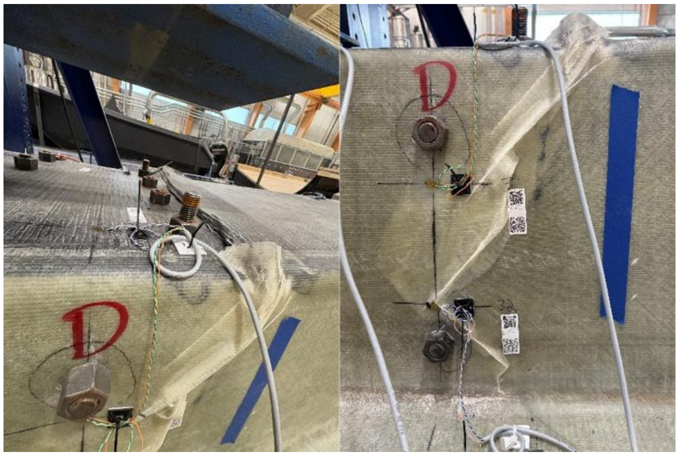

Figure 12: Buckling of the compression flange and fracture of the web near the west bulkhead

Figure 13: Smaller compression failure near the east bulkhead

A section of the specimen consisting of the compression flange and webs on the west side was removed to inspect internal damage. After removing only the compression flange, the web ridges and concrete splice remained bonded (refer to Figure 14). In Figure 14 it can also be seen that the concrete ridges in the compression flange/splice interface failed. While this damage could have been due to removal of the compression flange, the average shear stress at final failure computed per Eq. 1 with a moment at the specimen midspan of 2286 kN-m corresponding to the third failure load of 1416 kN is 6.39 MPa. This exceeds the strength of 4.12 MPa observed in the shear block tests using the Maine DOT deck concrete and A325 fasteners (Davids et al., 2022b) by 55.1%. If the moment at the bulkhead (end of the splice) of 1643 kN-m corresponding to a load of 1416 kN is used to calculate the average shear stress at failure, this gives a value of 4.59 MPa, which exceeds the assumed strength of 4.12 MPa by 11.4%. These results indicate that the concrete ridges at the flange interface could have failed during loading and not due removal of the compression flange. They also indicate that designing for the average interface shear stress computed using the moment at centerline pier may be overly conservative, and the moment at the bulkhead (end of splice) gives a better prediction of capacity. The FRP ridges remained intact in both the compression flange and webs, which is consistent with prior shear block tests (Davids et al. 2022b) and expected since the shear strength of the resin is greater than that of the concrete.

(a) Compression flange removed

(b) Compression flange and webs removed

Figure 14: Failed specimen after removal of the compression flange and webs

An external inspection of the failed specimen showed that the compression flange buckling occurred near the bulkhead at 111.8 cm to the west of mid-span and at 112.4 cm to the east of mid-span. Removal and inspection of the compression flange in the west side showed that its bottom (interior) surface failed at 117.8 cm from mid-span, and buckling resulted in a diagonal failure plane through the thickness of the compression flange. Although no visible damage was found in the compression flange ridges or the web FRP ridges as mentioned, delamination of the FRP was observed near the top of both webs (refer to Figure 15). The damage in the webs took place near the end of the splice where the compression flange failure was observed (refer to Figure 12) and may have been caused by large web deformations and strains initiated by compression flange buckling.

Based on the nominal specimen properties and the specimen design detailed earlier, the expected failure mode was flexural, with tensile yielding of the deck reinforcement followed by concrete crushing at mid-span. However, discussed later in the context of measured strains, the tensile reinforcement yield strength was apparently higher than nominal. This resulted in the specimen reaching an overall higher-than-expected load and the primary failure load shifting to compression flange buckling. Equation 7 predicts a critical local buckling loads per width of compression flange of 3.37 kN/mm, and 3.93 kN/mm is predicted if web rotational restraint is accounted for (Eqs. 2-6). Dividing by the compression flange thickness of 25 mm (refer to Table 1) gives critical buckling stresses of 134.8 MPa and 157.3 MPa for these conditions, respectively. For comparison, the average compression flange stress in the bare FRP section at the end of the splice is predicted to be 151.8 MPa at the first failure load of 1348 kN based on a transformed section analysis with a fully cracked concrete deck. This value is within 11.2% of the critical predicted buckling stresses of 134.8 MPa, and 3.5% below 157.3 MPa. This good agreement indicates that Eqs. 2-6 and Eq. 7 give very reasonable predictions for the compression flange buckling stress. Further, the simplicity of Eq. 7 and its tendency toward a slight degree of conservatism support its usefulness in design.


(a) North web (b) South web

Figure 15: Delamination of the top of north and south web

5.3 Specimen Flexural Strains

The measured flexural strains from no load to first failure for all functioning strain gauges are organized by sections and gauge locations as follows: tension bar gauges in the deck (Figures 16-19), girder gauges (Figures 20-22), all gauge data until first failure for all sections throughout the specimen (Figure 23) and all the compression bar gauges in the joint (Figure 24). Results from the following gauges are unavailable due to gauge failure: one TTC1, one CBD1, one BTD1, one BTB1, three BTA, one BTB2, one BTC2, one CBD2, and two BTD2 gauges. All failed gauges were located on the concrete reinforcement and could not be replaced after the concrete was poured.

Consistent and repeatable strain readings throughout the specimen were observed for all Service I cycles. Figures 16 and 17 illustrate rapid increases in strain on the tension rebar at loads of 600 – 1000 kN for sections C and D, which can be attributed to deck cracking. The jumps in strain at different load levels suggest that the deck did not crack uniformly. For the C sections, the east part of the specimen near C_1 cracked first at approximately 625 kN, followed by the west part at 1000 kN. For the D sections, the west part near D_2 cracked first at around 650 kN, while the east part cracked at 800 kN. Cracking in the concrete deck at different load levels can be attributed to inherent inhomogeneity of the concrete and the variability in concrete tensile strength. Further, since discrete cracks did not occur exactly at instrumented cross-sections, their impact on measured strains is not symmetrical along the span.

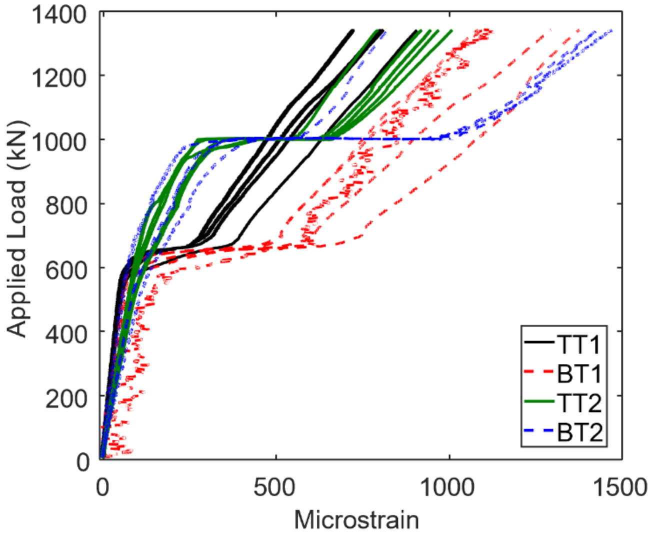

Figure 16: Tension rebar gauge data until first failure for section C

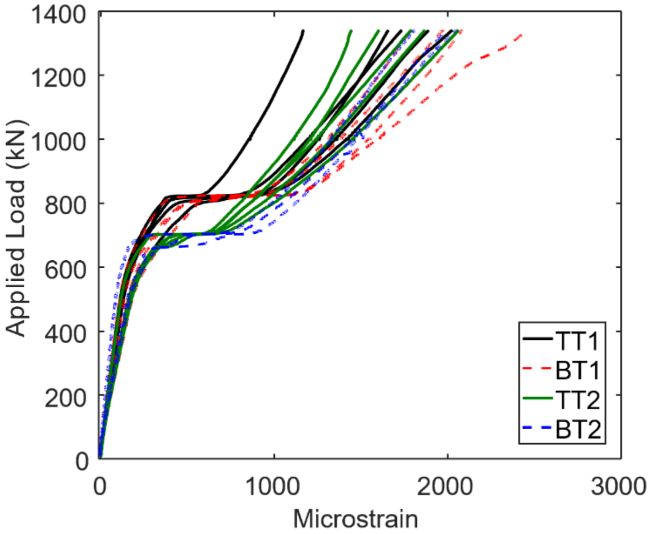

Figure 17: Tension rebar gauge data until first failure for section D

In contrast, the absence of such sudden strain increases in sections B and A (refer to Figures 18 and 19) suggests that cracking occurred earlier at lower loads. This agrees with the small amount of softening in the load-strain response in sections B and A that was observed during the first Service I cycle but not in subsequent cycles. The fact that strains in the tension reinforcing did not increase rapidly with small load increments after the nominal flexural capacity M_n for the reinforced concrete section A was reached at a load of 1117 kN (see Figure 19) suggests that the steel reinforcement did not yield. The maximum strain observed in the deck rebar of 2700 $\mu\epsilon$ corresponds to a stress of 540 MPa if the steel remained linearly elastic, which is consistent with widely available Grade 550 rebar. These observations indicate that it is likely that a higher Grade 550 material was substituted for the specified Grade 413 rebar.

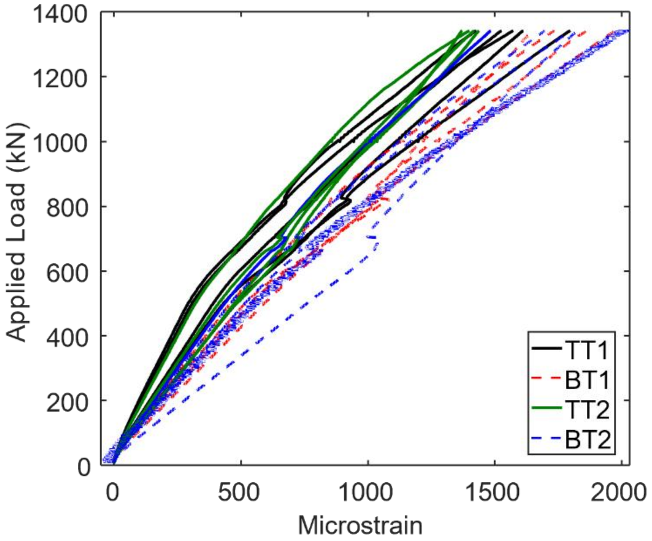

Figure 18: Tension rebar gauge data until first failure for section B

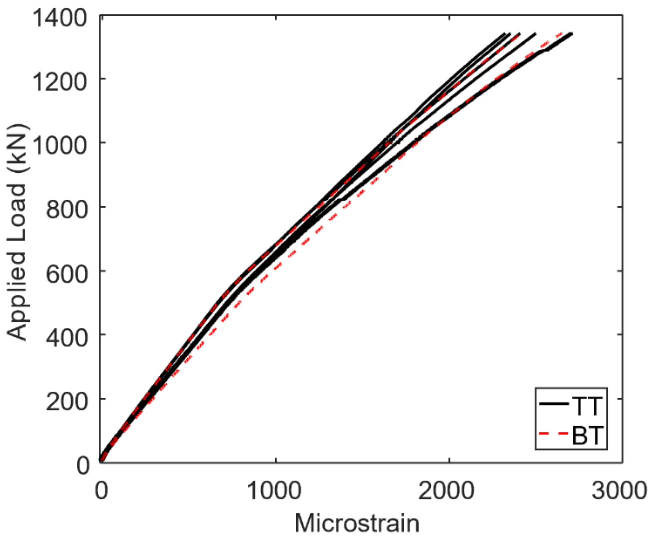

Figure 19: Tension rebar gauge data until first failure for section A

Figures 20-22 illustrate the FRP strains, and taken together reveal how the continuity joint and concrete infill influenced the strain distribution by taking part of the stresses that otherwise would have been carried by the compression flange. In the C sections, where only the girder and deck are present, the FRP displays the best example of a linear response (refer to Figure 20). As illustrated in Figure 21, strains are consistent at both D sections. At actuator loads of around 650 kN for the west side and 800 kN for the east side, both the rebar and the FRP strains reflect the influence of deck cracking in strain redistribution. In the case of the girder gauges, this is the most pronounced for the bottom flange, which shows sudden drops in tensile strain in the BF gauges at these loads. A similar shift can be seen in Figure 22 for the B sections where the strains at both the BW and BF locations appear to be affected by deck cracking. This suggests an increase of the influence of the concrete infill on the strain distributions closer to the midspan.

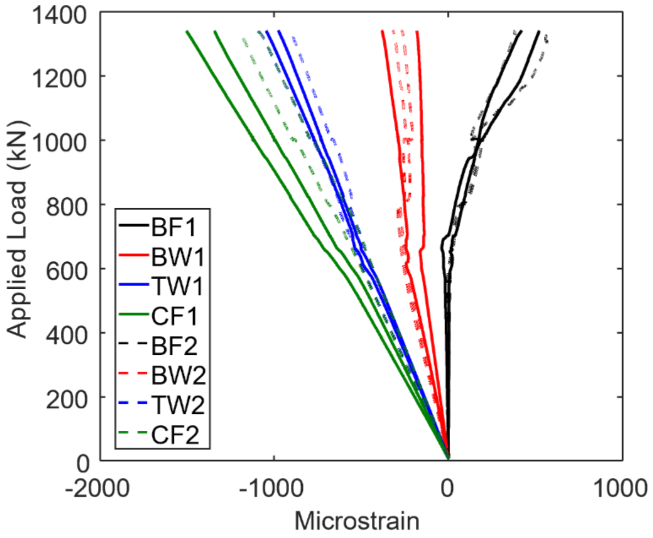

Figure 20: Girder gauge data until first failure for section C

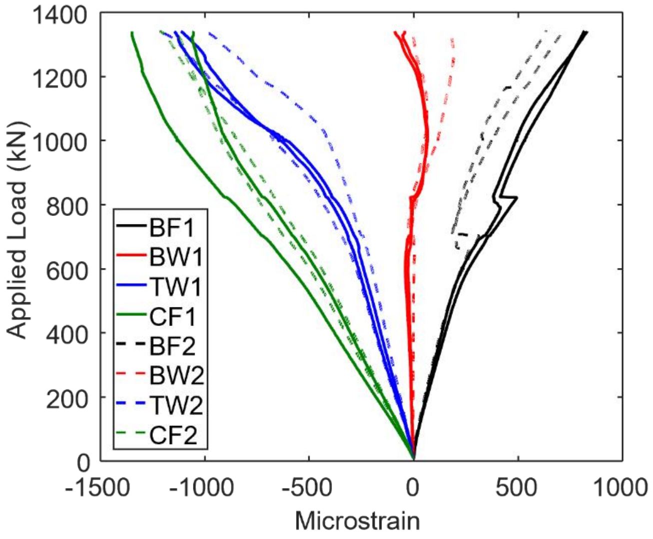

Figure 21: Girder gauge data until first failure for section D

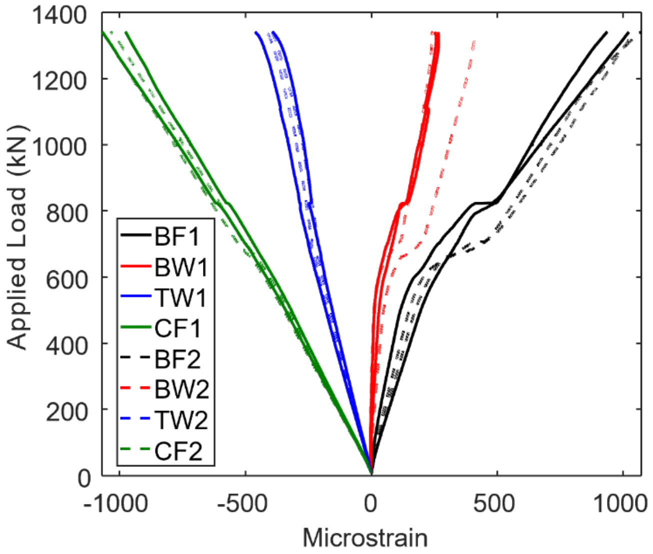

Figure 22: Girder gauge data until first failure for section B

To further highlight influence of the concrete infill, Figure 23 shows the variation in strain along the span at the first failure load of 1348 kN at different locations in the specimen. These results imply that the neutral axis shifted up the section due to the presence of the concrete infill, and that the splice also altered the cross-sectional strain distribution as the infill concrete began to carry compressive stress. While the compression flange strain at first failure was similar in magnitude at sections C and D, the moment due to the actuator load at section D was 60% greater than that at section C. There is a more rapid decrease in the magnitude of the bottom flange FRP compressive strain between sections D and B at first failure even though the applied moment is larger at B. Consistent with this is an even larger decrease in compression strain at the TW gauges over the same region at the first failure load, and the BW gauges shift from carrying significant compressive strains at section C to very small compressive or tensile strains at sections D and B. In contrast, the strain in the compression reinforcing is modest at section D (about -200 $\mu\epsilon$), but this increases in magnitude to about -800 $\mu\epsilon$ at section A (refer to Figure 24).

To further assess the influence of the concrete splice, strains in the FRP girder compression flange were computed using transformed section analysis assuming contributions from just the FRP girder and the rebar (i.e., the deck was assumed to be cracked at first failure load level). This gives strains of -1376 $\mu\epsilon$, -2202 $\mu\epsilon$ and -2477 $\mu\epsilon$ for sections C, D, and B, respectively. The experimental results for section C_1 closely agree with the theoretical strain at first failure with a difference of only 3.4%, which is expected since C_1 is outside the infill region. For sections D and B, the experimentally observed strains were 46% and 58% less than these values, respectively, which further shows the large impact of the concrete infill on the compression flange strains.

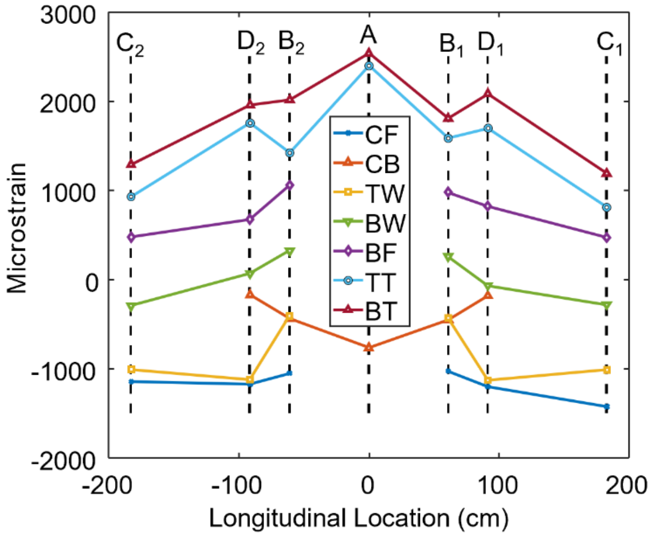

Figure 23: All gauge data until first failure for all sections throughout the beam

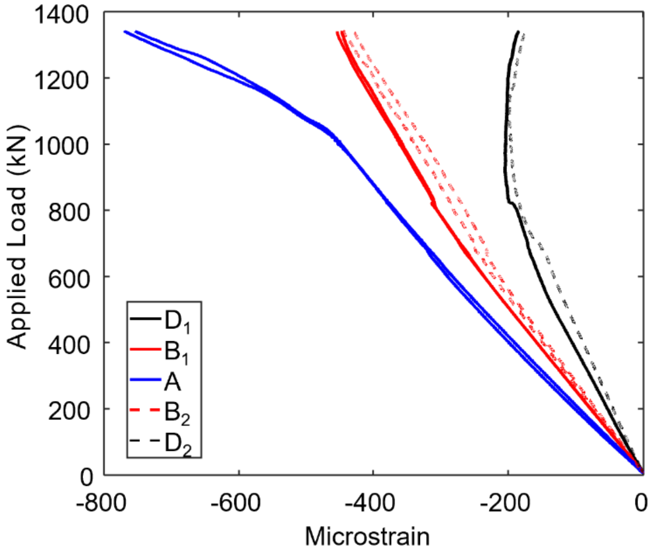

Figure 24: Compression rebar gauge data until first failure for all

Chapter 6: Comparison between Predicted and Measured Response

Figure 25 shows the variation in strain over the girder depth at sections C obtained using transformed section analysis along with experimentally measured strains. Best-fit lines were generated using average strain measurements from all gauges at the same vertical position. The results from both sections C_1 and C_2 were averaged to determine the strain profile at the Service I load (472 kN) and at first failure (1348 kN). The experimental results, despite the small deviation of certain values, are consistent with the assumption of a plane section remaining plane for linear elastic materials. At 472 kN, the best-fit line based on the measured strains indicates that the neutral axis lies is 200 mm from the section bottom, and at 1348 kN, it is 366 mm from the bottom. Elastic section analysis predicts a neutral axis position at 172 mm and 361 mm for loads of 472 kN and 1348 kN, respectively, which agree reasonably well with the values inferred from the experiment and confirming full composite action between the girder and concrete deck. Even though some deck cracking must have occurred before Service I, it was neglected when calculating the strain profile at 472 kN, and the deck was again assumed to be completely cracked when calculating it for first failure load level.

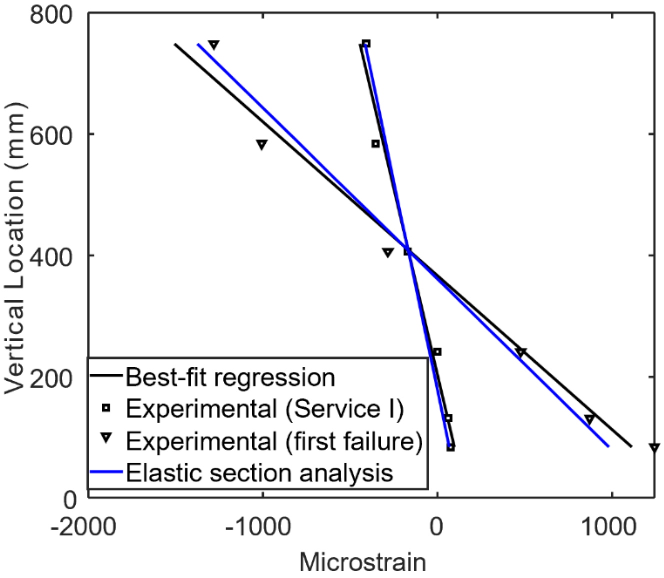

Figure 25: Section C strain profile for Service I (472 kN) and first failure (1348 kN) load levels

Although it is accurate to treat FRP components as linearly elastic, the concrete's potential for nonlinear behavior under high compressive strains required a more detailed model to accurately capture concrete stresses at mid-span. To accomplish this, the parabolic concrete constitutive model proposed by Desayi and Krishnan (1964) – specified for the flexural analysis of concrete members strengthened with externally bonded FRP reinforcement (AASTHO 2012) – was employed using the measured concrete compressive strength of 51 MPa. A moment-curvature analysis was performed for the reinforced concrete cross section at mid-span in which the contribution of the diaphragm was neglected and only the concrete area equivalent to the girder cross-section was accounted for. Neglecting the diaphragm will tend to under-predict the distance between the bending tension and compression resultants and give higher estimated concrete compressive stresses for the same applied moment.

Assuming a plane section and using the three measured strains in section A at the first failure and linearly extrapolating gives a strain at the top fiber of -1579 $\mu\epsilon$. This indicates that the concrete did not reach its crushing strain during the test, although it was well beyond its linearly elastic limit given that peak strength typically occurs at a strain of about -1800 $\mu\epsilon$ for normal strength concrete. The moment-curvature analysis estimates a total strain of -1599 $\mu\epsilon$ at the top of the concrete section at midspan. Figure 26 summarizes the three measured strains and the strains predicted using moment-curvature analysis. The neutral axis based on the experimental data and moment-curvature analysis is 499 mm and 486 mm from the bottom of the section, respectively. Overall, the moment-curvature analysis shows good agreement with the experimental strain data at section A.

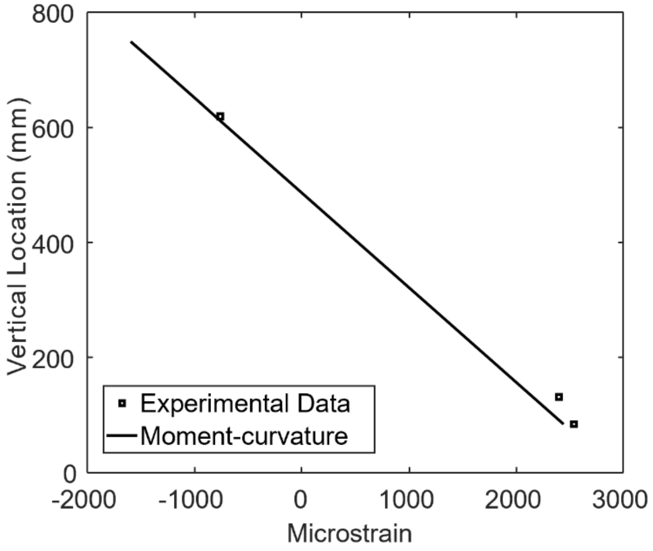

Figure 26: Section A extended strain profile and strain profile predicted from moment-curvature analysis at first failure

Chapter 7: Practical Impact of Live Load Continuity

The results of the experiment and subsequent analyses have demonstrated the feasibility of the proposed live load continuity joint. Here, parallel designs of the 30.48 m long, two-span continuous model bridge and a 30.48 m long bridge constructed of two 15.24 m long simply supported spans are investigated to quantify the positive benefits of the live load continuity joint for a practical scenario. For all conditions, the same six-girder cross-section shown in Figure 4a is assumed. The girder web and flange dimensions, properties and zones of the CT girder given in Table 1 apply for the continuous two-span bridge previously designed as the model structure. Further, for the continuous two-span bridge Zone 1 was applied over 183 cm at each exterior support, while the length of Zone 3 was fixed at 330 cm at the center pier and Zone 2 covered the remaining 11.76 m of each span. For the simply supported bridge, girder dimensions and properties were modified to meet design requirements as discussed below. Further, Zone 2 constituted the 11.58 m middle portion of the simple span and Zone 1 applied for 183 cm at each support, which is typical for currently deployed CT girder bridges. In all cases, deflection governed design, and girder positive flexural and shear strengths determined using current practice as detailed in Davids et al. (2024) and Schanck et al. (2023) exceeded Strength I demands.

The two-span continuous bridge with the section properties listed in Table 1 and girder dimensions given in Figure 4b is predicted to deflect 1.44 cm due to live load, meeting the requirement of $span/1000$ = 1.52 cm for a vehicular bridge that also carries pedestrians (AASHTO 2024). However, the simple span bridge with the same cross-section exhibits a maximum mid-span live load deflection of 3.89 cm, which significantly exceeds the 1.52 cm maximum. To ensure that the simple span bridge satisfies the deflection requirement, two options were considered. For Option 1, the depth of the FRP section was increased while maintaining the compression flange thickness of 25 mm and the other properties given in Table 1. For Option 2, the depth of the FRP cross-section was increased, and the thickness of the compression flange was also increased up to a maximum of 51 mm. The additional compression flange thickness is obtained by adding unidirectional carbon fiber layers to maximize E_1 and thus the section bending rigidity. Practice has shown that flange thicknesses greater than 51 mm can be challenging to successfully infuse, and were not considered practical.

Figure 27 summarizes the section dimensions for Options 1 and 2, and the original two-span section is also shown for visual comparison. A CT girder depth of 99.1 cm is required to limit deflection to 1.51 cm for Option 1. This gives an overall span to depth ratio of 12.8, which is 37% less than the 20.3 required for the two-span continuous bridge with the original cross-section. For Option 2, if the compression flange thickness is increased to the maximum feasible value of 51 mm the required CT girder depth becomes 72.4 cm to meet deflection requirements. This configuration results in an overall span to depth ratio of 16.4, which is 19% less than that of the two-span continuous bridge. Option 2 also requires a volume of unidirectional bottom flange carbon FRP of 0.4 m^3 per girder, which is 250% greater than the 0.16 m^3 per girder required for the 2-span continuous bridge and Option 1. Overall, these results illustrate clear gains in structural efficiency and material economy due to the live load continuity joint.

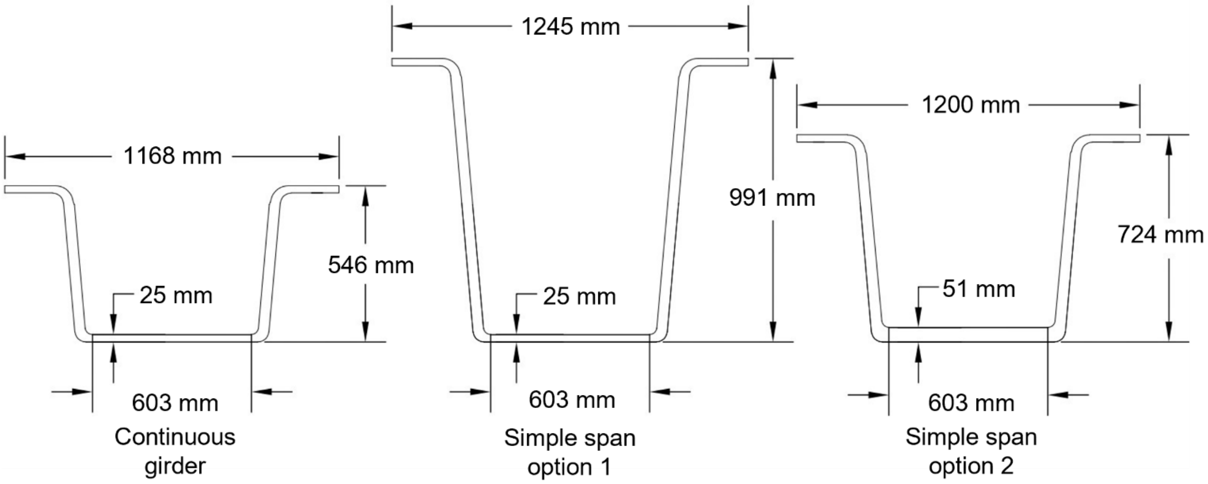

Figure 27: Girder cross-sections for three design conditions

Chapter 8: Summary and Conclusions

This paper has presented the development and experimental assessment of a novel live load continuity joint for FRP composite tub (CT) highway girders. The continuity splice relies on a conventional reinforced concrete section to carry moments caused by live load and superimposed dead load at piers, and does not require any bonded connection to transfer stress between FRP girders. The hollow girder section is filled with conventional deck concrete over a short portion of the span on both sides of the pier, and compression is transferred from the CT girder to the concrete infill via shear friction. The splice is straightforward to fabricate, requiring little additional work to fabricate since the girder serves as a stay-in-place form. A design method is proposed that allows the calculation of the required concrete infill length using basic mechanics principles and the concrete-FRP interface shear strength determined from results of compression-shear tests reported in a prior study. A specimen mimicking a full-scale splice in a two-span continuous, 30.48 m long bridge was designed, fabricated and tested to assess its flexural capacity following the application of approximately 500,000 cycles of an AASHTO Fatigue II loading. The specimen's ultimate strength exceeded its nominal flexural capacity based on the reinforced concrete section by 19.6%, likely due to the unintended inclusion of tension reinforcing with a higher-than-specified yield strength. Strain data indicated good bond between the concrete infill and girder as well as effective transfer of compression stress from the CT girder bottom flange to the concrete. Finally, a design example quantified the increase in efficiency gained when the continuity joint is used in a typical two-span CT girder bridge. Significant conclusions from this study are as follows.

- The performance of the splice was generally consistent with design assumptions, and shear stresses at the FRP flange-concrete interface at failure exceeded the average interface shear capacity obtained from prior compression-shear tests by as much as 55.1%. Measured strains clearly indicated that the compressive stress in the FRP section was effectively transferred to the concrete infill. Overall, the test results support the reasonableness of the splice configuration and design method proposed here. However, the specimen excess capacity indicates that the design might be conservative. This is consistent with ignoring interface shear transfer between the webs and concrete infill and sizing the splice length based on the peak moment at centerline pier as opposed to the smaller moment at the end of the concrete infill. Indeed, the average FRP flange-concrete shear stress at failure based on the moment at the end of the splice infill was much closer to the expected average interface shear capacity, exceeding it by only 11.4%. This gain could be due to the confinement of the concrete infill by the FRP section which will tend to improve concrete compressive and interface shear strength.
- Specimen strength was governed by local buckling of the compression flange. While this was not a controlling limit state in the specimen design, this does verify that compression flange buckling must be checked for any future bridges employing this live load continuity joint. An available analytical solution for the critical buckling stress of the flange used in the specimen closely predicted the flange compressive stress at failure derived from the test results. The test results indicate that the simplest analytical solution, which assumes that the webs provide no rotational restraint to the edges of the bottom flange, can be adopted for design with an acceptable degree of conservatism.
- The design example comparing the efficiency of a two-span continuous CT girder bridge with an equivalent structure composed of two simple spans showed clear advantages for the two-span bridge. The simple span structure required a reduction in span-to-depth ratio of 37% relative to the two-span continuous bridge if the bottom flange dimensions are held constant, which would severely limit available clearance in many practical situations. Further, if the span-to-depth ratio is reduced by 19%, the simple span bridge requires 250% more unidirectional carbon per girder on the compression flange for the same CT girder cross-section and spacing.

Taken as a whole, this study illustrates the efficacy and practical benefits of the proposed CT girder live load continuity joint. However, given that only a single specimen was tested and it exhibited higher-than-predicted capacity, additional research is justified. In particular, experimental and computational studies should focus on quantifying the relationship between capacity and splice length, better understanding shear strength of interface between the girder and concrete infill, and refining the proposed design methodology. Additionally, future research should explore the use of FRP shear connectors and FRP concrete reinforcing to reduce or eliminate the use of corrosion-prone materials in the live load continuity joint.

Chapter 9: Acknowledgements

This work was supported by the MaineDOT and University of Maine Transportation Infrastructure Durability Center (TIDC) under grant number 69A3551847101 from the US Department of Transportation’s University Transportation Centers Program.

Chapter 10: References

AASHTO. (2018). *AASHTO LRFD Bridge Design Guide Specifications for GFRP-Reinforced Concrete (2nd ed.)*. Washington, DC: AASHTO.

AASHTO. (2024*). AASHTO LRFD bridge design specifications (10th ed.)*. Washington, DC: AASHTO.

AASHTO. (2012). *Guide Specification for Design of Bonded FRP Systems for Repair and Strengthening of Concrete Bridge Elements.* AASHTO: Washington, DC, USA.

AASHTO. (2012). *Guide Specification for Design of Concrete-Filled FRP Tubes for Flexural and Axial Members.* AASHTO: Washington, DC, USA.

AASHTO. (2008). *Guide Specification for Design of FRP Pedestrian Bridges*. AASHTO: Washington, DC, USA.

American Concrete Institute. (2017). *Guide for the Design and Construction of Externally Bonded FRP Systems for Strengthening Concrete Structures* (ACI PRC-440.2-17). American Concrete Institute: Farmington Hills, MI, USA.

American Concrete Institute. (2015). *Guide for the design and construction of structural concrete reinforced with FRP bars* (ACI 440.1R-15). Farmington Hills, MI: ACI.

Bai, Y., and Keller, T. (2008). Modal parameter identification for a GFRP pedestrian bridge. *Composite Structures*, 82(1):90-100.

Bakis, C. E., Bank, L. C., Brown, V. L., Cosenza, E., Davalos, J. F., Lesko, J. J., & Triantafillou, T. C. (2002). Fiber-reinforced polymer composites for construction—State-of-the-art review. *Journal of Composites for Construction*, 6(2), 73–87.

Benmokrane, B., El-Salakawy, E., El-Ragaby, A., and Lackey, T. (2006). Designing and testing of concrete bridge decks reinforced with glass FRP bars. *Journal of Bridge Engineering*, 11(2):217-229.

Bentz, E. C., Massam, L., & Collins, M. P. (2010). Shear strength of large concrete members with FRP reinforcement. *Journal of Composites for Construction*, 14(6), 637–646.

Burgueño, R. (1999). System Characterization and Design of Modular Fiber Reinforced Polymer (FRP) Short- and Medium-Span Bridges. Doctoral Dissertation, University of California, San Diego.

Cao, Y., Liu, M., Zhang, Y., Hu, J., & Yang, S. (2020). Effect of Strain Rates on the Stress–Strain Behavior of FRP-Confined Pre-Damaged Concrete. *Materials*, 13(5), 1130.

Davids, W.G., Diba, A., Dagher, H.J., Guzzi, D., and Schanck A. (2022a). Development, assessment and implementation of a novel FRP composite girder bridge. *Construction and Building Materials*, 340(2022):127818.

Davids, W.G., Guzzi, D., and Schanck, A. (2022b). Development and experimental assessment of friction-type shear connectors for FRP bridge girders with composite concrete decks. *Materials*, 15(2022):3014.

Davids, W. G., Schanck, A., & Clark, J. (2024). Flexural capacity and fatigue performance of full-scale FRP-concrete composite highway bridge girders. *Structures*, 69 (2024) 107401.

Desayi, P., & Krishnan, S. (1964). Equation for the stress-strain curve of concrete. *Journal of the American Concrete Institute*, 61(3), 345–350.

Fam, A. and Honickman, H. (2010). Built-up hybrid composite box girders fabricated and tested in flexure. *Engineering Structures*, 32(2010):1028-1037.

Freyermuth, C. L. (1969). Design of continuous highway bridges with precast, prestressed concrete girders. *PCI Journal*, 14(2), 14–39.

Gutierrez, E., Mieres, P.S., and Calvo, J.M. (2008). Structural testing of a vehicular carbon fiber bridge: Quasi-static and short-term behavior. *Journal of Bridge Engineering*, 13(3):271-281.

Honickman, H. and Fam, A. (2009). Investigating a structural form system for concrete girders using commercially available GFRP sheet-pile sections. *Journal of Composites for Construction*, 13(5): 455-465.

Jendli, Z., Meraghni, F., Fitoussi, J., & Baptiste, D. (2009). Multi-scales modelling of dynamic behaviour for discontinuous fibre SMC composites. *Composites Science and Technology*, 69(1), 97–103.

Karbhari, V.M., Seible, F., Burgueño, R., Davol, A., Wernli, M., and Zhao, L. (2000). Structural characterization of fiber-reinforced composite short- and medium-span bridge systems. *Applied Composite Materials*. 7(2000):151-182.

Kassem, C., Farghaly, A. S., & Benmokrane, B. (2011). Evaluation of flexural behavior and serviceability performance of concrete beams reinforced with FRP bars. *Journal of Composites for Construction*, 15(5), 682–695.

Li, Y-F., Badjie, S., Chen, W. W., & Chiu, Y-T. (2014). Case study of first all-GFRP pedestrian bridge in Taiwan. *Case Studies in Construction Materials*, 1, 83–95.

Ma, L., Liu, F., Liu, D., & Liu, Y. (2021). Review of Strain Rate Effects of Fiber-Reinforced Polymer Composites. *Polymers*, 13(17), 2839.

Maine Department of Transportation. (2018). Bridge design guide (2003 ed., updated June 2018). Augusta, ME: MaineDOT.

Mendes, M.A., Barros, J.A.O., Sena-Cruz, J.M., and Taheri, M. (2011). Development of a pedestrian bridge with GFRP profiles and fiber reinforced self-compacting concrete deck. *Composite Structures*, 93(11):2969-2982.

Mieres, J., I. Calvo, L. Pineda, F. Botello, M. Gomez, S. Primi and J. Bonilla. 2007. "First bridge constructed of carbon fibre reinforced polymers in Spain." in *FRPRCS-8*, Patras, Greece

Miller, R. A., Castrodale, R. W., Mirmiran, A., & Hastak, M. (2004). *Connection of simple-span precast concrete girders for continuity*. NCHRP Report No. 519: Transportation Research Board.

Nejad, A. F., Salim, M. Y., Koloor, S. S., Petrik, S., Yahya, M. Y., Hassan, S. A., & Shah, M. K. (2021). Hybrid and Synthetic FRP Composites under Different Strain Rates: A Review. *Polymers*, 13(19), 3400.

Oesterle, R. G., Glikin, J. D., & Larson, S. C. (1989). *Design of precast-prestressed bridge girders made continuous (NCHRP Report No. 322)*. Transportation Research Board, National Research Council.

Okeil, A. M., & Alaywan, W. (2011). *Evaluation of Continuity Detail for Precast Prestressed Girders.* Louisiana Transportation Research Center.

Pinkham, J., Davids, W.G., and Schanck, A. (2024). Assessment of moment live load distribution in FRP composite tub girders for highway bridges. *Journal of Bridge Engineering*, 29(5):04024024.

Pinkham, J., Davids, W. G., Schanck, A., & Berube, K. (2025). Distribution of live load shears in FRP composite tub girder highway bridges. *Engineering Structures*, 322, 119188.

Saadeghvaziri, M. A., Spillers, W. R., & Yin, L. (2004). *Improvement of Continuity Connection over Fixed Piers*. New Jersey Department of Transportation.

Sá, M. F., Silvestre, N., & Costa Neves, L. F. (2017) Dynamic Behaviour of a GFRP-Steel Hybrid Pedestrian Bridge in Serviceability Conditions. Part 1: Experimental Study. *Thin-Walled Structures*, 117, 332–342.

Schanck, A., Davids, W., Pinkham, J., & Berube, K. (2023). Assessment of web shear stresses and shear capacity of FRP composite tub girders for highway bridges. *Structures*, 880-894.

Siwowski, T., and Rajchel, M. (2019). Structural performance of a hybrid FRP composite lightweight concrete bridge girder. *Composites Part B: Engineering*, 174(2019):107055.

Siwowski, T., Rajchel, M., Kaleta, D, and Własak, L. (2017). The first Polish road bridge made of FRP composites. *Structural Engineering International*, 2(2):308-314.

Skinner, J.M. (2009). A critical analysis of the Aberfeldy footbridge, Scotland. *Proceedings of Bridge Engineering 2 Conference 2009*. Bath, UK.

Qiao, P., & Zou, G. P. (2002). Local Buckling of Elastically Restrained Fiber-Reinforced Plastic Plates and its Application to Box Sections. *Journal of Engineering Mechanics*, 128(12), 1324–1330.

Zhang, C., & Abedini, M. (2023). Strain Rate Influences on Concrete and Steel Material Behavior, State of the Art Review. *Archives of Computational Methods in Engineering*, 30:4271–4298.

TIDC

Transportation Infrastructure Durability Center
AT THE UNIVERSITY OF MAINE

35 Flagstaff Road
Orono, Maine 04469
tidc@maine.edu
207.581.4376

tidc.umaine.edu